Nanostructure Tuning of Gold Nanoparticles Films via Click Sintering

Massimo Urban, Giulio Rosati,* Gabriel Maroli, Flavio Della Pelle, Andrea Bonini, Laszlo Sajti, Mariangela Fedel, and Arben Merkoçi*

Colloidal metal nanoparticles dispersions are commonly used to create functional printed electronic devices and they typically require time-, energy- and equipment-consuming post-treatments to improve their electrical and mechanical properties. Traditional methods, e.g. thermal, UV/IR, and microwave treatments, limit the substrate options and may require expensive equipment, not available in all the laboratories. Moreover, these processes also cause the collapse of the film (nano)pores and interstices, limiting or impeding its nanostructuration. Finding a simple approach to obtain complex nanostructured materials with minimal post-treatments remains a challenge. In this study, a new sintering method for gold nanoparticle inks that called as "click sintering" has been reported. The method uses a catalytic reaction to enhance and tune the nanostructuration of the film while sintering the metallic nanoparticles, without requiring any cumbersome post-treatment. This results in a conductive and electroactive nanoporous thin film, whose properties can be tuned by the conditions of the reaction, i.e., concentration of the reagent and time. Therefore, this study presents a novel and innovative one-step approach to simultaneously sinter gold nanoparticles films and create functional nanostructures, directly and easily, introducing a new concept of real-time treatment with possible applications in the fields of flexible electronics, biosensing, energy, and catalysis.

1. Introduction

Colloidal gold has been used for health treatments and art for thousands of years. In 1875, Michael Faraday found a way to produce it synthetically,[1] and since then, photonic, catalytic, and other properties of gold in its nanometric structure have been studied and used in numerous fields.[2–6] The versatility of this material has been exploited creating nanofunctional surfaces by inkjet printing taking advantage of the colloidal stability of gold nanoparticles (AuNPs) dispersions. In the last few years, nanostructured materials have been commonly integrated in biomedical devices, demonstrating tremendous improvements in their analytical performance.[7–9] Nanostructured electrodes have thus garnered a lot of attention for their potential as effective transducing elements for the detection of a wide range of biomarkers, but also for catalysis and energy storage among other applications.[10–12] There are several approaches for the electrochemical performance enhancement via

M. Urban, G. Rosati, G. Maroli, F. D. Pelle, A. Bonini, A. Merkoçi
Nanobioelectronics and Biosensors Group
Catalan Institute of Nanoscience and Nanotechnology (ICN2)
Campus UAB, Bellaterra, Barcelona 08193, Spain
E-mail: giulio.rosati@icn2.cat; arben.merkoci@icn2.cat

M. Urban
Doctorado en Biotecnología
Universitat Autònoma de Barcelona
Campus de la UAB, Bellaterra, Barcelona 08193, Spain

F. D. Pelle
Department of Bioscience and Technology for Food, Agriculture, and Environment
University of Teramo
Campus "Aurelio Saliceti" via R. Balzarini 1, Teramo 64100, Italy

A. Bonini
Department of Chemistry and Industrial Chemistry
University of Pisa
via Giuseppe Moruzzi 13, Pisa 56124, Italy

L. Sajti, M. Fedel
Nano-Engineering Group
RHP Technology GmbH
Seibersdorf 2444, Austria

A. Merkoçi
Catalan Institution for Research and Advanced Studies (ICREA)
Passeig de Lluís Companys, 23, Barcelona 08010, Spain
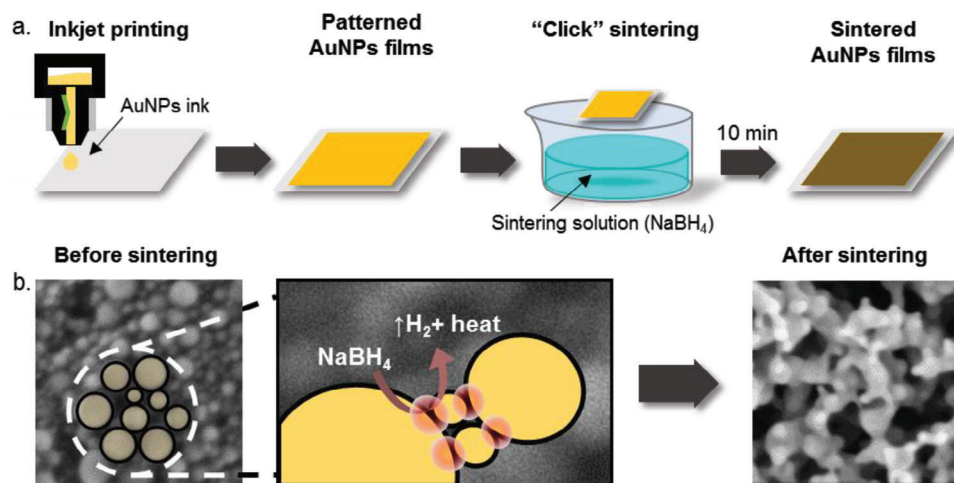
Figure 1. Overview of the fabrication of the devices, from inkjet printing to click sintering. a) Scheme of generic printing and sintering protocol for AuNPs inkjet-printed films; b) illustrative representation of the sintering mechanism involving the reaction with the sintering agent (NaBH$_4$) and the local nanoenviroment at the interphase.

nanostructuration, including the decoration of the electrodes' surface with NPs, electroplating, or the fabrication of the entire transducer with metal nanoparticles (MNPs).[3,6,13–15] In alternative to MNPs depositions, other classical approach to create homogeneous nanoporous gold network include, chemically or electrochemical dealloying, template-assisted depositions, etching, and chemical depositions.[14,16,25–28,17–24]

Despite several options available, there are few methods allowing the low-cost, efficient, and easy fabrication of nanostructured metal-based conductive surfaces, and even less on flexible or deformable plastics and paper substrates.

In the last decade, inkjet printing using MNPs inks has become a popular fabrication technique in the fields of flexible electronics and biosensing.[29–32] Compared to other printing techniques, inkjet printing offers higher resolution, reduced use of solvents, and freedom and flexibility in terms of layouts. After deposition, the printed films typically undergo a process called sintering. Sintering is a thermodynamically induced growth process that increases the dimensions of MNPs, leading to a smaller surface-to-volume ratio, less surface chemical potential, and higher overall stability.[33] The process leads to conductive paths in MNPs-based films and starts with the curing of the deposited film, starting from the removal of the solvent and reaching the removal of the capping agent, which hinders the electrical/electrochemical response.[34–36] Immediately after, the real sintering process starts, forming junctions between the MNPs creating conductive paths, and improving the film's mechanical strength.[37–39] Generally, this causes the collapse of the porous structure of the nanoparticle interphase and the consequent loss of the film nanostructure.

The selection of the appropriate sintering process for inkjet-printed films is based on the type of ink, the printing substrate, and on eventual time/scalability-related requirements. For example, in mass fabrication lines, a photonic approach is usually preferred, but the most typical way is via thermal annealing.[38,40,49,41–48] Flexible electronics and biosensing applications are often based on temperature-sensitive substrates such as plastics or paper; hence, alternative strategies to thermal treat-

ment are required. In this direction, chemical approaches have also been explored to induce sintering of printed nanomaterials, including gases, ionic compounds, and salts, sometimes using cumbersome procedures with difficult (or impossible) industrial implementation or losing the inherent nanostructure properties of the nanoparticles.[50–55] In this context, chemically induced sintering of noble MNPs inks remains an important challenge.

In this study, we propose a straightforward method called "click" sintering for tuning the nanostructure of AuNPs conductive films, compliant with paper and polymeric substrates. The method consists in an instantaneous reaction at the AuNPs particle interphase, of a solution of sodium borohydride (NaBH$_4$) at room temperature (**Figure 1**b). We have observed that the NaBH$_4$ treatment of AuNPs films modulates the nanostructuration, giving improved electrochemical features and making possible the easy fabrication of ad-hoc electrodes/surfaces for various applications, such as electrochemical biosensors, Surface Enhanced Raman Scattering (SERS) substrates, gas sensors, flexible electronics, and wearable devices.[56] The proposed method does not require any equipment and can be performed virtually in any lab in just a few minutes. Furthermore, we demonstrated that the process can be automated via integration into an inkjet printer.

2. Results and Discussion

In this work, we have shown that the concentration of NaBH$_4$ modulates the nanostructuration of AuNPs films, improving electrochemical properties, and giving them a peculiar optical activity, as will be described in the next paragraphs. This click-sintering method takes advantage of the nanochemical phenomena occurring on the surface of the NPs, i.e., a catalytic exothermic reaction inducing the formation of a nanoporous surface of metal NPs. NaBH$_4$ has already proved to be effective in removing thiols, polyvinylpyrrolidone (PVP), and other ligands from colloidal gold and other metal NPs,[57,58] however, to the best of our knowledge there is no report about its use as nanostructuring sintering agent for AuNPs-based inks in printed electronics and nanobiosensing.

**ADVANCED
SCIENCE NEWS**

www.advancedsciencenews.com

**NANO · MICRO
small**

www.small-journal.com
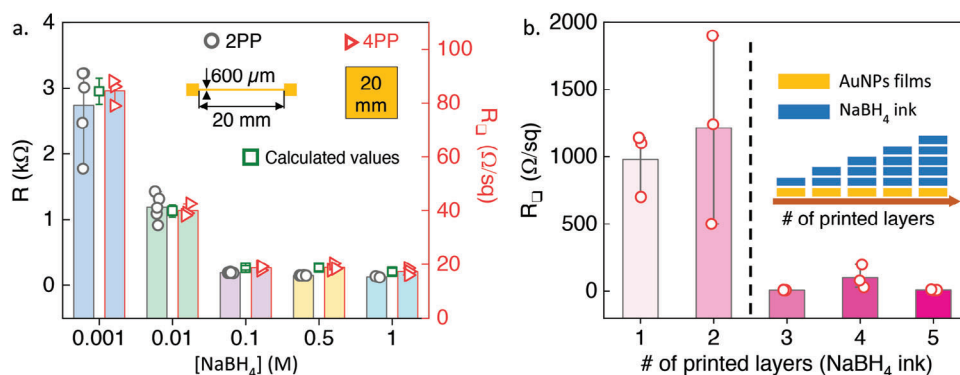
Figure 2. Electrical characterization of the inkjet-printed gold films produced via dipping (a) and via inkjet sintering (IJS) (b). a) Sheet resistance values for the AuNPs-ink printed squares (in red) and resistance values of the printed lines (in black), after the 10 min treatment with different concentrations of $NaBH_4$; the squares represent the calculated resistance using the sheet resistance and the aspect ratio of the trace. The top right insets in the two plots show the layouts of the respective printed structures. b) Sheet resistance values for the 20 mm squares, after real-time inkjet sintering on Kapton® at increasing numbers of layers, it is showed a threshold in the relative amount sintering solution ($NaBH_4$ 0.5 M ink). The columns represent average values and the bars the respective standard deviations (n = 3).

Herein, AuNPs-films conductivity, nanostructure morphology, elemental composition, and the material's surface chemistry were investigated after this simple click sintering treatment to shed light on its mechanism and to define the properties acquired by the film. Additionally, the film's electrochemical features have been studied using two different redox molecules (e.g., methylene blue and ferro/ferricyanide) to pave the way for potential applications in flexible electronics and electrochemical nanobiosensing.

2.1. Electrical Characteristics of the Nanostructured Films

To prove the effectiveness of the sintering process we evaluated changes in the film sheet resistance, resistivity, and conductivity. Two-wire (2P) and four-point probe (4P) methods were used to measure both the resistance of printed lines and the sheet resistance of the film. Simple lines (20 mm long and 600 μm wide) and 20 mm side squares were printed on a commercially coated PET substrate via inkjet printing with a consumer printer. The inkjet-printed films appeared gold-colored after printing but resulted non-conductive, as expected in absence of a sintering treatment. The AuNPs-films were then treated by immersion in 0.05 M NaOH solutions containing different concentrations of $NaBH_4$ for 10 min, ranging from 1 mM to 1 M. The films were then rinsed with MilliQ water and dried with nitrogen.

The sheet resistances of the squares and the resistances of the lines have been measured for each concentration of $NaBH_4$. A decrease in the resistance was observed with increasing concentrations of $NaBH_4$ for both the tested printed layouts (**Figure 2**a). The pristine untreated films did not result conductive; thus, they do not appear in the plots. Figure 2b shows the resistivity obtained for inkjet sintering (IJS), performed by placing the $NaBH_4$ solution (0.5 M) in a dedicated cartridge of the printer, and performing different passages (named layers) onto the inkjet printed AuNPs-film on Kapton substrate (Figure S1, Supporting Information).
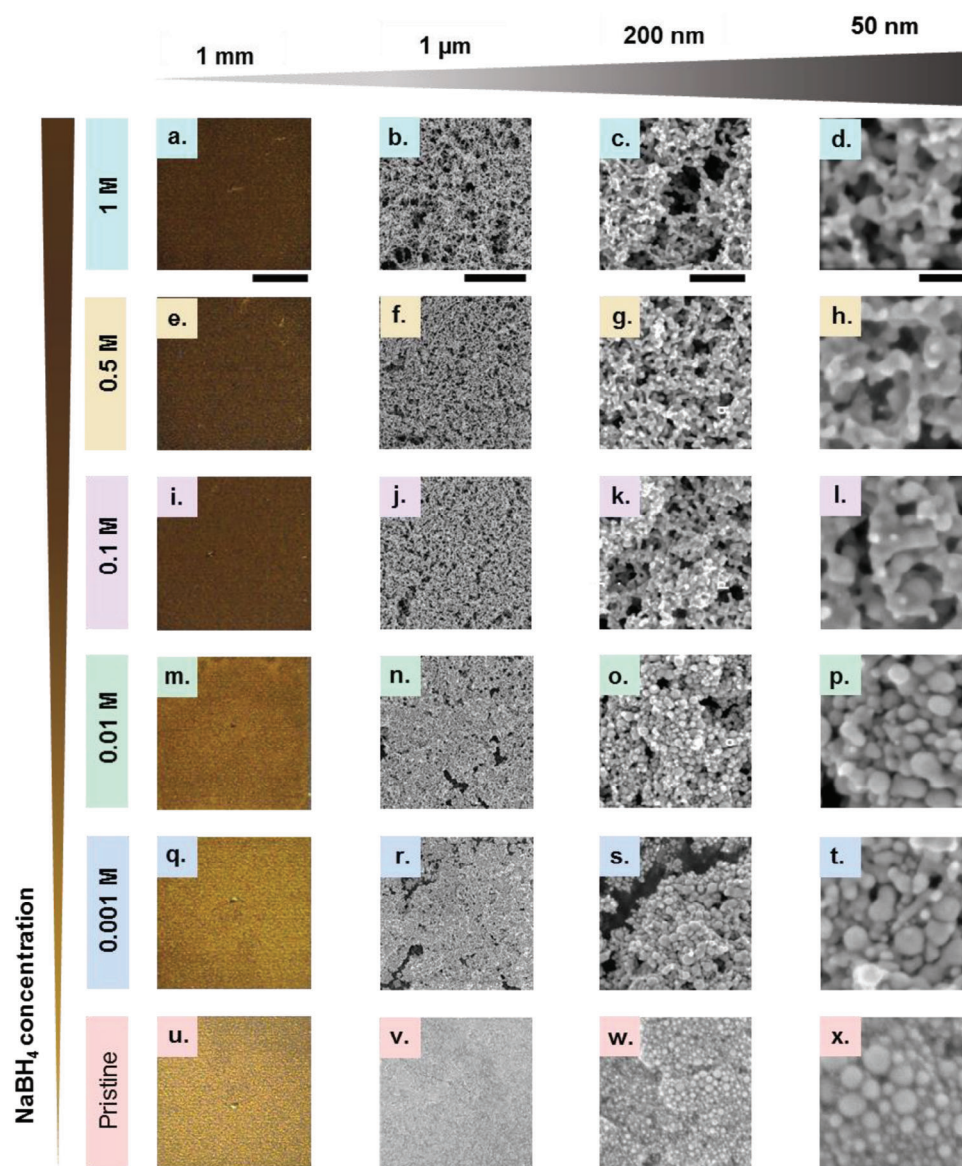
In Figure 2a, a decrease of the (sheet) resistance has been evidenced with concentrations lower than 0.1 M $NaBH_4$, with an

excellent correlation between the two measurements (see SI for the calculation). We used the average thickness of the film printed over Mitsubishi substrate (Figure S2, Supporting Information), combined with the measured sheet resistance, to calculate the conductivity and resistivity. A concentration of $NaBH_4$ 1 M proved to be the best value in terms of resulting electrical performance, with a conductivity of $5.14*10^7$ S m^{-1}, equivalent to 1.25% of the bulk conductivity of gold ($4.11*10^7$ S/m). Although the value is not particularly high, compared with the state-of-the-art AuNPs inks and printed films, this places our method somewhere in the middle in term of performances, but with a clear advantage in terms of time, temperature of the process and with the result of an extended nanostructuration (Tables S1 and S3, Supporting Information).

While performing the alternative sintering method, i.e., using inkjet printing, the sheet resistance remains high and not reproducible, indicating a heterogeneous treatment, up to two $NaBH_4$ printed layers (Figure 2b). With three layers or more, a sharp decrease in resistivity has been evidenced with a higher degree of reproducibility. Given the small volume deposited with the IJP process, multiple layers are therefore necessary for an effective sintering of the films. We found that three layers of sintering agent per layer of AuNPs ink produced the best result. Noteworthy, the resistivity obtained with IJS turns out to be similar to the one obtained via dipping.

Nanostructure. The colors and morphology of the printed films after the click sintering with different $NaBH_4$ concentrations are reported in **Figure 3**. From a macroscopic point of view, the treatment produced a gradual change in the color of the gold film, from gold to deep brown, proportionally with the $NaBH_4$ concentration (Figures 3a,e,i,m,q,u).

The SEM micrographs demonstrate that the nanostructure significantly varies with different concentrations of the sintering agent. The untreated AuNPs film shows a uniform distribution of spherical NPs on a dense underlying layer, whereas a dense 3D-network with cavities and pores extending over the whole nanostructure is observed with $NaBH_4$ concentrations over 0.1 M (Figure 3g–l,m–r). This effect could be linked to the necking process that occurs during the sintering after

**ADVANCED
SCIENCE NEWS**
www.advancedsciencenews.com

NANO · MICRO
small
www.small-journal.com

Figure 3. The chemical sintering at different concentrations tunes the proprieties of the gold films from the micro to the nanometric scale. First column reports the optical pictures of the films treated with different concentrations of NaBH$_4$, showing the color variations from yellow to dark brown. Second, third, and fourth columns, SEM images at increasing magnifications of the sintered AuNPs-film treated with different concentrations of NaBH$_4$. Scale bar dimension from left to the right 1 mm, 1 μm, and 200 and 50 nm.

the capping layer removal. This process creates junctions between NPs, making the film conductive (they "click"), and increases the porosity and nanostructure of the film, resulting in a higher surface-to-volume ratio. TEM micrographs confirm the formation of the neck between the particles (Figure S2, Supporting Information). This process can be described as a catalytic-induced sintering of NPs, which occurs without the need for external sources of energy. The intrinsic chemical energy of the reaction is harnessed, confined to the nanodomains of the solid-state film triggering the sintering and forming a web-like structure. To our knowledge, this is the first report about catalytically induced sintering as a tunable nanostructuration mechanism.

NaBH$_4$ is a promising reagent for hydrogen production in both solid and liquid phases, and its dissociation in water has been well-studied in the literature.[59–61] Alkaline pH stabilizes NaBH$_4$, by reversing the equilibrium of the hydrolysis in water.[62,63] Noble metal catalysts have been used to dissociate NaBH$_4$ in an exothermic reaction, which produces hydrogen gas.[60,64,65] The proposed mechanism involves intermediate species where formal hydride is bonded to the surface of the particle and then reacts with water in the rate-determining step.[60] When gold films are exposed to the sintering solution, a visible color change accompanies the production of hydrogen gas that is especially intense at higher concentrations of NaBH$_4$ (Figure S3b and Video S2, Supporting Infromation). SEM images reveal the presence
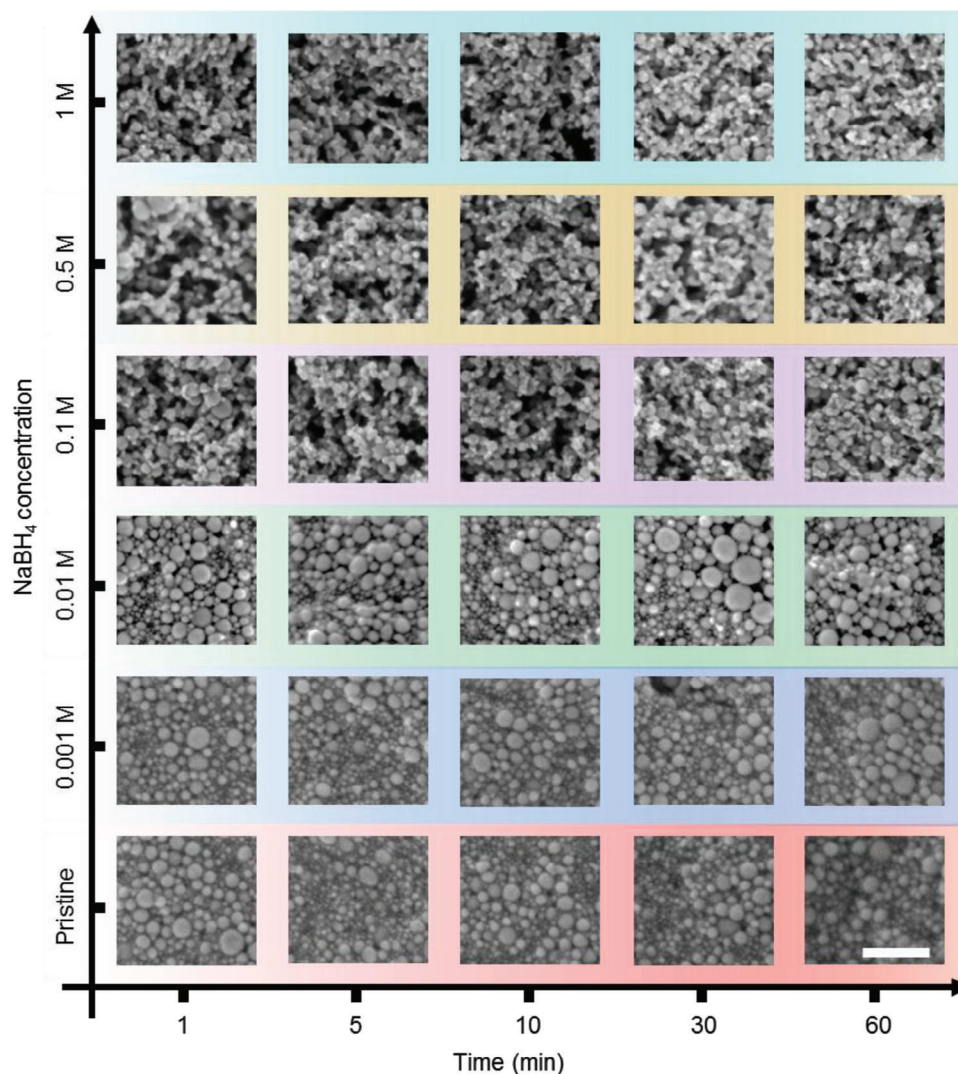
Figure 4. Time-concentration SEM study of the morphological effects of the NaBH₄ via dip sintering. Changes in morphology have been monitored at different concentrations for times spanning from 1 to 60 min. As in the previous figure, 0.1 M appears as the threshold concentration NaBH₄ for triggering an extended nanostructure change. Conversely, time does not appear to have an evident effect on the morphology, as it has been observed also during the inkjet sintering (see Figure 2), which is a real-time process. Scale bar 200 nm.

of cavities and pores in the printed structure that can only be explained by the micro-explosions of hydrogen gas produced in the deeper regions of the film (Figure S4, Supporting Information). The rate of the catalytic reaction, and therefore hydrogen production, is heavily affected by the concentration of NaBH₄. At lower concentrations, the NPs undergo competition between hydrogen production and energy production via exothermic reactions, leading to their coalescence. The sintering process occurs rapidly, and the morphology doesn't change significantly within 1 h (**Figure 4**). It is widely accepted that there is a relationship between the activity of the catalyst and particle size, with smaller particles being increasingly more active compared to the bigger-sized ones.[66] We speculate that the smaller particles, which are nested between the larger ones, are the main actors in the reaction. This is suggested by the "fishing net" structure that forms with bigger particles connected to each other and separated by smaller NPs and narrow necks. The network-forming process

stops when thermodynamic equilibrium is reached, i.e., when desorption/reabsorption of PVP reaches balance and all the active crystalline planes of the smaller particles have reacted.

The coalescence modes of the AuNPs change according to the NaBH₄ concentration, with two main driving forces, i.e., i) de-capping rate and ii) spatial confinement. We think that the most probable way for it is that the hydrogen produced during the reaction interacts with the PVP via destabilization and mechanical removal, most probably following a similar reaction occurring during the electrochemical cleaning of the gold electrodes via oxidations and subsequent reductions.[67] With higher concentrations of sodium borohydride (≥0.1 M) the PVP destabilization rate is higher, and the removal of the capping agent results almost instantaneous, or in the range of seconds (Figure 4). The arrangement of the AuNPs in the film is ruled by the printing, the drying process, and the substrate surface properties, forcing the NPs into defined positions. During the sintering the NPs start
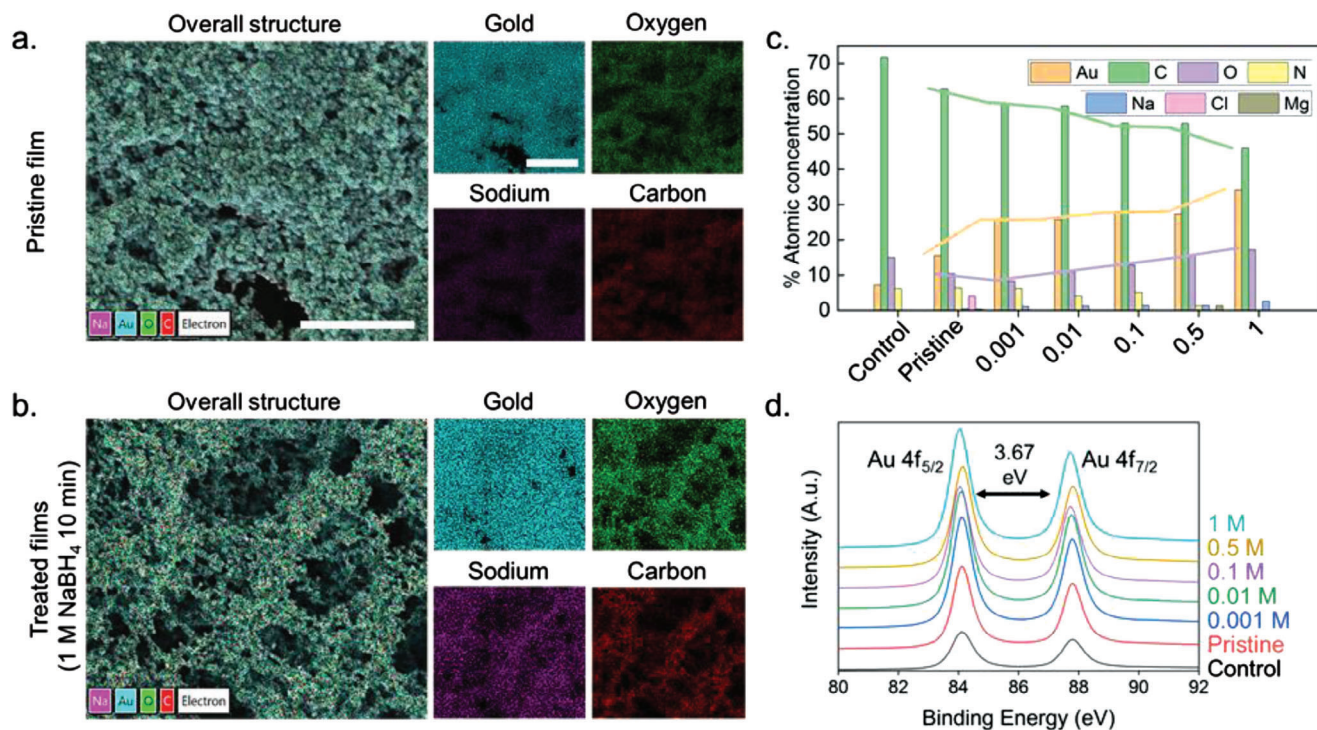
Figure 5. Physiochemical characterization of the printed AuNPs films at the different concentrations of the sintering agent. a) EDX maps of the pristine and of the 1 M NaBH$_4$ treated devices with the compositional maps showing the distribution of the main elements found (Au, O, Na, and C). The overall nanostructure rearrangement with the increased porosity is evident in the overall structure. However, the single elements do not show relevant alterations. b) The atomic concentrations of the elements (Au, C, O, N, Na, Cl, and Mg) evidence of an increase in the gold content and a decrease of the carbon one with increasing NaBH$_4$ concentrations. No contaminants were evidenced on the surface of the treated films. c) The XPS measurements of the gold 4f$_{5/2}$ and 4f$_{7/2}$ peaks showed a constant separation, and d) the intensities do not appear to change proportionally with the NaBH$_4$ concentration. Scale bar 500 nm.

necking in all directions, toward the closest NPs, creating a 3D porous network, with a larger degree of freedom close to the surface. Analyzing the bottom layers of the film, a more compact structure can be appreciated (Figure S5, Supporting Information). The situation is similar in the case of inkjet sintering (IJS) where the nanostructure changes after reaching a threshold number of layers, i.e., 3 (Figure S6, Supporting Information). For low concentrations (or jetted volumes for the IJS) of sodium borohydride, the destabilization of the PVP capping layer results slower, with no apparent change on the film surface, despite making it conductive. The discrete nature of the printing process, depositing the sintering agent layer-by-layer, allows for selectively tuning the structure by using an appropriate number of layers.

2.2. Composition and Chemical State

Energy-dispersive X-ray Spectroscopy (EDX) and X-ray Photoelectron Spectroscopy (XPS) analysis allowed the identification of the main components and chemical state of the gold film surfaces, their distribution, and their percentage variations in response to the treatment with NaBH$_4$ (**Figure 5**).

The different elements present after the treatment of the film are reported on the elemental maps (Figure 5a,b) and the XPS survey (Figure S7, Supporting Information). The distribution of the analyzed elements in the sampled area (gold, carbon, oxy-

gen, and sodium) appears uniform and homogenous. The XPS shows that the surface concentrations of carbon and nitrogen are decreasing with increasing concentrations of NaBH$_4$, as an effect of the PVP capping agent removal. It is to be noted that no boron is present on the surface of the film, contrary to what was expected using an excess of reagent. Metaborate products produced during the reaction are soluble in water and negatively charged, as the NPs used in this work (ζ-potential −40 mV in water see Table S5, Supporting Information). The electrostatic repulsion explains the absence of the boron species and the appearance of Na, which is positively charged and tends to accumulate on the surface, increasing with the concentration of NaBH$_4$. The high-resolution XPS spectra of the Au 4f show the doublets corresponding to the photoemission peaks of the 4f$_{5/2}$ and 4f$_{7/2}$ orbitals, at binding energies of 87.79 and 84.12 eV, respectively, with a peak-to-peak distance of 3.67 eV. The result is coherent with the NPs being in the metallic form with formal oxidation state Au^0.[68] Both the distance and the position of the peaks remain constant with the treatment. The peak intensities change accordingly to the extent of the removal when the concentration of NaBH$_4$ is increased. The absence of variation in the gold peak suggests that no relevant interaction between the gold and the sodium borohydride takes place, with no change in the formal oxidative state of the gold due to the treatment. The examination of the deconvolution of the carbon peaks provides insights into possible reactions or interactions with the polymer. It has been

ADVANCED
SCIENCE NEWS
www.advancedsciencenews.com

NANO · MICRO
small
www.small-journal.com

reported that PVP has different binding modes on metal NPs, depending on the size, length of the chain, and branching.[69,70] Given the broad size distribution of the AuNPs used in this work (polydispersity index>0.1) it is reasonable to expect a contribution coming from the different binding modes of the polymer. For other metals, the interaction with the charge transfer with the polymer translates into additional components in the XPS peak model as formal species with charge +1, related to the chemisorption of the oxygen onto the metal surface.[71–73] However, this is not what was observed (Figure S8, Supporting Information). The ratio between the components related to the Au (0) and the Au (I), does not change during the different treatments, and remains constant even after changes in concentration of several orders of magnitude. The carbon peaks also remained constant and did not change significantly after the treatments at different concentrations, further confirming that NaBH$_4$ interacts directly only with the particles and with no other species (Figure S9, Supporting Information). A closer inspection reveals that the peak of the amidic carbon progressively shifted toward lower binding energies at lower concentrations of NaBH$_4$ but returned to its normal position at higher concentrations, suggesting an increase in the surface of the NPs where the PVP has been displaced but not bonded. It is possible to propose different interpretations of this phenomena: i) according to Ansar et al,[57] we found that the substitution of the PVP with hydride does not affect the gold oxidation state, and no change in the electronic shell of the Au can be detected; ii) the NaBH$_4$ interacts directly with the NPs, producing hydrogen and mechanically detaching the coordinated PVP, as it has been demonstrated in the mechanism related to the electrochemical cleaning with sulfuric acid.[67,74] The higher concentrations of the sintering agent also modulate the nanostructuration, with distinctive electrochemical and optical proprieties, such as the color change caused by the change in the scattering properties of the material due to the newly-formed nanostructure.[23,75]

The morphological change of the surface with the treatment could explain the color variation of the films ,[76,77] because of its different light absorbance. These data prove that the color changes of the films are not imputable to chemical changes of the film but are due to changes in the nanostructure. SERS measurements also offer a view of the effects of the nanostructuration. Rhodamine was used as a probe, and the intensity of its characteristic peak (1626 cm^{-1}) was taken as a reference signal.[78,79] The intensity of the Rhodamine 6G peak (1626 cm^{-1}) decreases linearly increasing the concentration of NaBH$_4$ after 0.01 M (Figure S10, Supporting Information). More nanostructured films showed higher porosity and irregular shapes (Figure 3). On average the distance and gaps between the NPs are larger, which implies fewer hot spots enhancing the Raman scattering. Numerous factors influence the SERS phenomena, such as the nature and the morphology of the metal on the substrate; among others, particularly significant is the assembling and the NPs shape.[79–81] In this case higher concentrations of sintering agents create more disorganized and porous structures with active centers distancing each other. This also opens the way to possible strategies of tuning the optical proprieties of the film changing the concentration, and possibly having a film that is conductive and at the same time optically active toward the SERS detection mechanism.

2.3. Electrochemical Properties

Cyclic voltammetry (CV) measurements in presence of ferro/ferricyanide as redox probe, have been performed to evaluate the electron transfer ability of the AuNPs electrodes treated with different concentrations of NaBH$_4$. A conductive film with poor electroactivity has been formed with the lowest NaBH$_4$ concentration, but already with 0.01 M NaBH$_4$, the electrochemical response showed a significant improvement, corresponding to the transition behavior between macroelectrode and nanostructured electrode (**Figure 6**).

Figure 6a clearly shows that the peak intensity increases, and the peak-to-peak separation decreases proportionally to the NaBH$_4$ concentration used for the treatment (Figure 6a,b). Furthermore, for all the electrodes, the peak currents varied linearly with the square root of the scan rate and with an anodic and cathodic peaks ratio corresponding to 1, in accordance with the Randles-Sevcik equation, showing the characteristics of a quasi-reversible reaction.[82] The electron transfer constant k_0, a value defining the efficiency of the redox process, increases linearly with the concentration of NaBH$_4$ due to the exposition of more redox active centers with the treatment (Table S2, Supporting Information). For the higher NaBH$_4$ concentrations, the peak currents in the CVs increase linearly with the scan rate, up to≈500 mV s^{-1} after which a small secondary shoulder at high potentials (≈0.45 V) appears. This shoulder peak could be attributed as a feature of nanoporous gold electrodes, due to the complex kinetics and diffusion typical for porous systems.[83]

We then performed CVs scans in 0.1 M sulfuric acid, and calculate the total electroactive surface area (ECSA) of the AuNPs, by extracting the area corresponding to the gold oxide reduction peak (≈0.7 V), knowing the theoretical consumed charge for polycrystalline gold (410 µC cm^{-2}) (Figure S13, Supporting Information).[67] This value can be normalized to the geometrical area, the roughness factor (R_f), calculated as the ratio between the effective area A$_{eff}$ and the geometrical area A$_{geo}$ (Figure 6d; Table S2, Supporting Information).
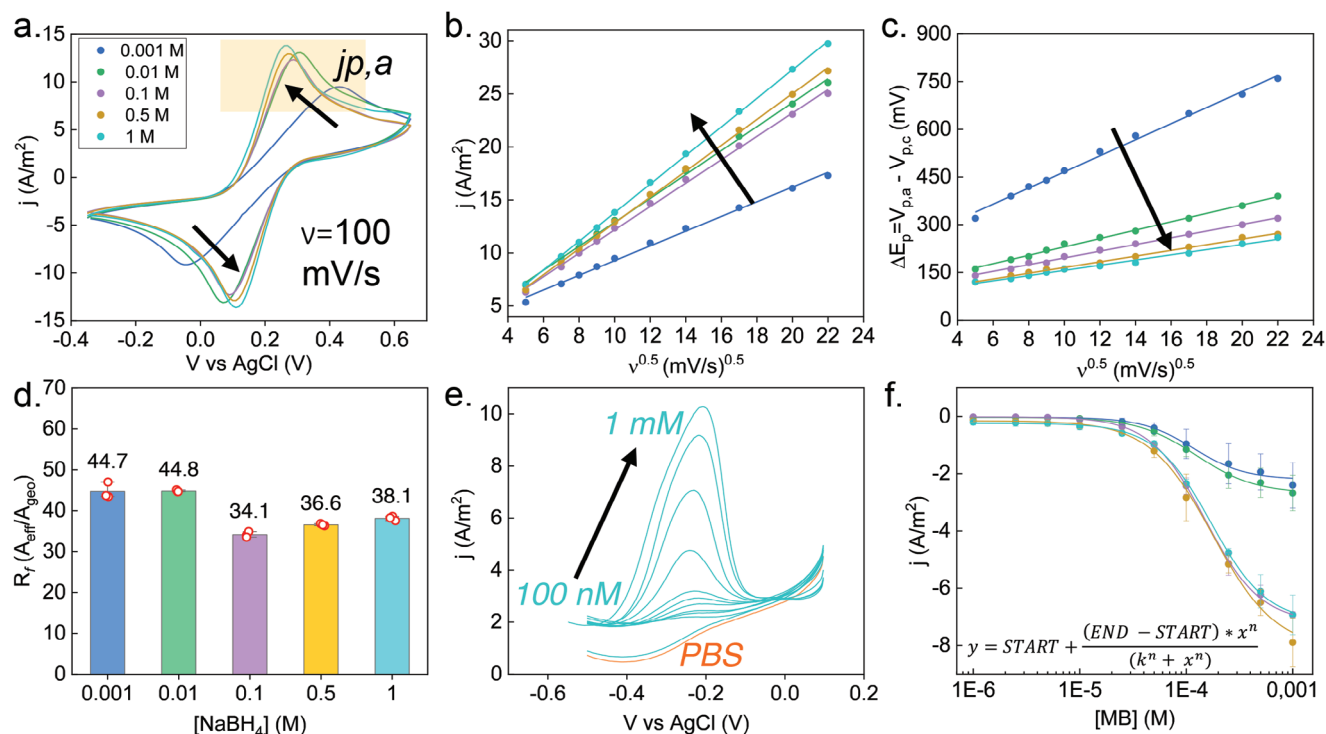
The R_f tops to a remarkable value of 40, comparable or even higher than some of the commonly used method for producing nanoporous gold, with the advantages and unique features of speed, temperature, and integration provided by our treatment (**Table 1**). The value decreases at the threshold NaBH$_4$ concentration of 0.1 M, where starts increasing again (Figure 6). This phenomena is correlated to the transition in morphology that happens at that specific concentration and clearly visible from the SEM analysis (Figure 3). The nanoparticles "click" together losing their sphere-like shape due to the sintering. This causes a loss of total surface area, because some of the crystalline planes available for the redox process coalesce forming new entanglements. It is also important to compare this value with the electrode transfer constant, k_0, calculated before. Even if with higher surface area, using lower NaBH$_4$ concentration, causes inefficient de-capping of the polymer layer. This causes the films to be higher in total surface area, but overall less sensitive to the redox probe (Table S2, Supporting Information), compared with the films treated with higher concentrations. Also, the differences in the areas calculated with the Randles-Sevick equation and the integration of the gold oxide peak in the CV in sulfuric acid, suggest us that not

Table 1. Comparison table of the main protocols for the fabrication of nanoporous gold.

Ref.	Protocol	Substrate	T_{max}/T_{nano} [a] [°C]	t [b] [h]	R_f [c]	Pore size [nm]	Reagents	Comments
[16]	Dealloying	Gold wire	120	2-3	540	100	$ZnCl_2$ in benzyl alcohol	Requires alloying
[17]	Electrochemical etching	Gold-disk electrode	RT[d]	<0.01	35	N.S.[e]	HCl 2M	None
[14]	Chemical deposition	MCE[f] membrane	60	2	7.3	N.S.	Au^{3+} solution in NH_2OH	Multiple cycles for total coverage of the paper
[18]	Drop casting	Gold electrode	RT	<10	300	N.S.	For AuNPs synthesis	Multiple casting is necessary
[19]	Template-assisted deposition	COP[g] resin	160/RT	2	N.S.	120	Many (for fabrication of the mold)	Metal is sputtered on the nanoimprinted mold
[20]	Photonic sintering	PET[h]	120/RT	20	N.S.	44-48	Many (for polymer synthesis)	Multiple steps for the polymer synthesis, assembly and removal.
[21]	Hydrogen-bubble method	GCE[i]	RT	0.02	135	30-50	H_2SO_4 and $AuCl_4^-$	Electrodeposition
[22]	Net shaping method	Cu wire tamplate	600/RT	96	N.S.	25-45	HNO_3, Cu and Au solution	Requires alloying step at HT. Electroplating/corrosion cycles.
[23]	Electrochemical	Si wafer	RT	0.3	32	N.S.	HF and DMF	Sputtering on chromium
[24]	Electro-deposition	C[j]	RT	0.1	14	N.S.	PB[k], AA[l] solution	Anodization followed by reduction of the gold oxide layer
[25]	Gold leafs	Kapton tape	RT	0.05	36.3	5-25	HNO_3	Deposition of the leaf, and selective etching via polymer mask.
[26]	Electrochemical etching	Au electrode	RT	0.1	8.5	N.S.	H_2SO_4	Electrochemical etching of the gold
[27]	Electrochemical+ Dealloying	Gold wire	600/RT	18	232	N.S.	HNO_3	Requires alloying, electrodeposition followed by dealloying
[28]	Metal-induced crystallization	GCE	110/RT	0.5	≈3	N.S.	H_2O_2	Deposition GCE via sputtering and chemical etching
This work	Click sintering	PET, Kapton	RT	<0.5	≈40	7-15**	$NaBH_4$	Deposition and sintering can be integrated in a consumer inkjet printer

[a] T_{max}/T_{nano} = maximum temperature of the process/ temperature for the step inducing the porosity; [b] t = time (time is calculated by considering the total time from the preparation of the sample to the step of nanostructuration; [c] R_f = roughness factor (A_{eff}/A_{geo}); [d] RT = room temperature; [e] N.S. = not specified; [f] MCE = mixed cellulose ester; [g] COP = cyclo-olefin polymer; [h] PET = polyethylene tereftalate; [i] GCE = glassy carbon electrode; [j] CD = compact disk; [k] PB = phosphate buffer; [l] AA = ascorbic acid; ** = see Supplementary Figure S16 (Supporting Information)

ADVANCED
SCIENCE NEWS
www.advancedsciencenews.com

NANO · MICRO
small
www.small-journal.com

Figure 6. Electrochemical characterization of the treated electrodes. a) Cyclic voltammetry measurements performed on 4 mm square AuNPs printed working electrodes with external Ag/AgCl reference and Pt counter electrodes in 5 mM ferro/ferricyanide in 10 mM phosphate saline buffer (PBS, pH 7.4, 23 °C). b) Anodic peak currents recorded versus the scan rate for the electrodes treated with different concentrations of $NaBH_4$. c) Peaks separation as a function of the scan rate for the treated electrodes. d) Roughness factor of the films at the different concentrations of chemical agent. e) SWV response of the films treated with 1 M $NaBH_4$ for concentrations of MB in PBS ranging from 100 nM to 1 mM. f) Calibration curve fitted with a Hill equation (inset) for the films treated with the different concentrations of the sintering agent (n = 3). SWV parameters: 25 Hz frequency, 25 mV amplitude, potential range from 0.1 to −0.4 V.

all the gold surface is active toward redox processes, and the click sintering at high concentrations enhances this aspect.

Finally, to approach the use of these electrodes as a substrate for biosensing, methylene blue (MB) was also used on the differently treated gold surfaces (Figure 6d–f). MB was chosen as a model probe since it is widely used as mediator and redox reporter in biosensing devices.[56,84] There is a clear change in the performance of the film once the sintering agent threshold concentration is reached (Figure S11, Supporting Information). The EC proprieties of the material change just slightly with a further increase of the concentration of $NaBH_4$ due to a more efficient decapping, rather than more extended nanostructural changes. The click-sintered electrodes allows to detect MB in solution in the low µM range using SWV, without any additional post-treatment.

2.4. Scalability, Integration, and Comparison

The method described in this work is divided in three steps: 1) ink loading; 2) film printing; 3) click sintering and washing. After the first step, 6 mL of the AuNP ink can be printed for the fabrication of up to 15–20 pages, each one containing around 130 electrochemical devices (Figure S14, Supporting Information). The rheological parameters, have been selected and modified according to a previously published work using commercial silver nanoparticles (AgNPs) ink, and proven to be printable with ac-

ceptable resolution and precision over Mitsubishi substrate and Kapton (Figure S15, Supporting Information).[85] We verified the ink is stable inside and outside the printer up to one month, with no sign of aggregation as shown from dynamic light scattering and UV–vis spectroscopy (the time was selected accounting our average usage of ink for fabricating electrodes) (Figure S15, Supporting Information). The simultaneous printing of AgNP inks for the reference electrodes and the contacts allow to perform the complete NPs film deposition in a single print (lasting less than 5 min). The sintering step is then performed in less than 10 min per page with the possibility to use the same solution for more pages. The washing is performed first in deionized water and afterward in milliQ water for less than 2 min. The method as it is can thus be easily scaled-up. A further improvement in this direction can be performed by adding the sintering agent as an ink in the inkjet printer and printing it on top of the gold electrodes in a second passage. We have verified that the alignment grants a good coverage of the electrodes and the waste of reagent is drastically reduced even if more than one passage is needed for a complete sintering (as shown in Figure 2b). With this method, despite the obvious advantages in terms of volume of sintering agent and precision of its deposition, the stability over time of the sintering agent in the consumer printer may be affected by eventual cross contaminations onto the printhead by residues of the AuNP ink. For this reason, the complete integration for further scaling-up of the method would be better achieved with ad-hoc designed

printers, preventing the ink mixing in the printhead cleaning phase, or simply by using two printers, the second one being exclusively dedicated to the sintering agent. In Table 1, we compare the results of our method with the main state-of-the-art protocols for the formation of nanoporous gold, and how our method drastically simplifies the process to obtain it in an additive, sustainable, easy, and rapid way at room temperature.

3. Conclusion

We introduced a novel sintering method that we call click-sintering, which enhances and tunes the nanostructuring of AuNPs films at room temperature. This unique and innovative strategy utilizes the internal energy produced during a catalytic exothermic reaction to induce the coalescence of NPs, resulting in a web-like nanostructured conductive gold surface. We propose a possible implementation of this technique integrating it into a consumer inkjet printer, providing an affordable strategy for one-step printing of nanostructured conductive substrates, without any post-treatment and opening the way to the use of sensitive and fragile substrates since no thermal treatments are needed after the film deposition. The potential applications for this technology are vast, including flexible electronics, energy, catalysis, and biosensing. We have thoroughly investigated the modulation mechanisms of the substrate's electrochemical properties mediated by the sintering process. Our findings show that the modes of coalescence behind the net-like structure are related to the de-capping mechanism of the polymer and the rates of how this phenomenon happens is strictly correlated to the nanochemical environment in the interphases between the particles. This study provides new insights about the complex sintering mechanism puzzle and opens alternative possibilities for the direct and straightforward fabrication and modulation of nanofunctional structures using an easy, cheap, and rapid methodology.

4. Experimental Section

AuNPs Ink Synthesis: Ultrapure, water-based AuNPs inks were synthesized via pulsed laser ablation in liquids by RHP-Technology with a single-step method enabling the synthesis of size-controlled and highly-stable colloids at room temperature and atmospheric pressure.[86,87] The laser system included an InnoSLab, nanosecond pulsed laser (IS400, Edgewave) delivering 7 ns full-half width maximum (FHWM) pulses at 1064 nm, at a repetition rate of maximum 10 kHz and pulse energy of 40 mJ. The laser beam was focused by a high-speed Galvo scanner (intelliSCAN III-10, Scanlab) through a telecentric 65 mm focal length F-θ quartz lens (S4LFT4065/328, Sill Optics). Spherical-shaped AuNPs with a mean diameter of 15 ± 5 nm were generated from a 99.99% pure gold target (Agosi AG) in a closed flow chamber whereas the laser beam was coupled horizontally into the process chamber. As liquid media, 1 L Type I. water (>18 MΩ cm, Milli-Q, Merck-Millipore) containing 0.01 mM polyvinylpyrrolidone (PVP10, Sigma Aldrich) was used, while a controlled liquid flow of 500 mL min^{-1} was generated by a non-contact tube pump (Heidolph, Hei-FLOW Precision 06) circulating the liquid between a liquid reservoir and the ablation chamber. Up-concentration of the gold colloid into a highly-stable nanoink was achieved by rotary evaporation (Hei-VAP Precision, Heidolph) (35 °C, 35 mBar, 140 rpm) to remove the excess water and to adjust the NP concentration. A water-based gold-ink with 26.5 wt.% solid particle content was thus obtained, that showed excellent long-term stability. The nanoink formulation was then adjusted to 15 wt.% AuNP concentration including 1.6 mM PVP capping agent in a printing solution composed of water (72%), ethylene glycol (25%), ethanol (2%), and iso-propyl alcohol (1%).

Device Fabrication: The gold inkjet-printed lines were fabricated using an Epson XP15000 consumer printer loaded with the 15% w/v AuNP nanoink. Six milliliters of the ink were loaded into an empty cartridge (supplier) already installed on the printer printhead (cyan channel). After the initial printhead cleaning, the observers waited one day before performing the nozzle check and starting the printing of the devices. Two different substrates were used for printing: transparent polyethylene terephthalate (PET) and Kapton. PET sheets in A4 dimension had a porous coating to allow the immediate drying of the AuNPs solvent and optimal adhesion (Mitsubishi Paper Mills NB-TP-3GU100). Both the printer and the substrate were selected in previous works.[85,88] Kapton sheets (Kapton KPC) were purchased from DuPont. The substrate was cut into A5 sheets and treated with 4 M NaOH to increase the surface wettability. The printed patterns were designed in Autodesk AutoCAD 2020 and were composed of two connection pads (3 mm x 3 mm) and 2 cm long 600 μm wide lines connecting them.

Click Sintering of AuNPs Films–Immersion Method: Sodium borohydride powder (purity 98% and MW of 37.83 g mol^{-1}) and sodium hydroxide pellet (purity>98%, 40.05 g mol^{-1} MW) were purchased from Merck, Sigma–Aldrich. Ultrapure MilliQ Millipore deionized water (18.2 MΩ cm^{-1}) was used for the preparation of the solutions. Sintering solutions were prepared dissolving NaBH$_4$ 0.001, 0.01, 0.1, 0.5, and 1 M in 0.5% sodium hydroxide to stabilize the sintering agent and slow down the decomposition reaction.[62,63] The films were transferred to glass Petri dishes immediately after preparation and immersed in the sintering solution for the selected time (10 min if not otherwise specified) at room temperature under shaking. The films were then dipped twice in Milli-Q water to stop the reaction and remove potential side products, dried with a towel to remove the water excess and with nitrogen until completely dried.

Inkjet Real-Time Click Sintering: Consumer printers had multi-ink (color) cartridges connected to a single printhead with separated nozzle arrays. The loading of the AuNPs in a color channel (e.g., cyan) and of the sintering agent in a second one (e.g., yellow) allows for the implementation of sintering of the printed AuNPs by printing the desired designs in mixed colors (e.g., green). The sintering ink was prepared by dissolving sodium borohydride in a solution containing 72% NaOH solution 0.5 M, 21% ethylene glycol, 2% Ethanol, and 1% isopropyl alcohol, to reach a final concentration of 0.5 M. The ink was loaded in the cartridge, which was inserted in the yellow channel housing, performing multiple prints on the gold films, drying after each printing, and performing the washing only after the desired number of layers were deposited. This was done for two reasons: first to increase the local concentration of the agent before, and second to mimic the situation of real-time printing and sintering where the sheets undergo multiple passes before being washed or used. The gold films, for sake of simplicity, were cut and attached to a paper sheet (Figure S3, Supporting Information) to be placed inside the printer.

Ink Properties Characterization–Rheological Properties: The viscosity of the ink was measured using an AMETEK Brookfield Viscometer for low torque ranges (CZ-40 spindle), performing a full scan at different shear speeds and fitting a linear curve extracting the viscosity from the slope of the curve. The measurements of the contact angle and the surface tension were performed by means of a Drop Shape Analyzer DSA25S (KRÜSS GmbH, Hamburg, Germany), using the sessile drop and pendant drop techniques, respectively. The drop shapes were analyzed in both cases with the KRÜSS ADVANCE software. For the analysis of the contact angles, drops of 2 μL were cast on the surfaces with an automatically software-controlled syringe and 0.5 mm diameter steel needles. In the case of the surface tension, the pendant drops were generated by an automatic software-controlled dosser in the tip of a 1.8 mm diameter steel needle.

Dynamic Light Scattering (DLS):   DLS and zeta potential measurements were performed with Zeta Sizer Nano ZS (Malvern Instruments), in disposable Zeta Sizer cuvettes using the automatic focus calibration and analysis. The measurements were performed every week for 1 month diluting 1 μL of the prepared ink into 1000 μL of water or water/ethylene glycol dispersion.

**ADVANCED
SCIENCE NEWS**

www.advancedsciencenews.com

NANO · MICRO

small

www.small-journal.com

UV–Vis: Absorbance spectra were acquired using a Plate Reader Spectramax I3, scanning from 400–800 nm with a 5 nm step, using an ELISA plate filled with 100 µL of different concentrations of gold ink diluted in MillQ water. A blank spectra of the MilliQ water was acquired and used as a baseline.

Surface Characterizations: Pictures of the printed lines were acquired by an Andostar ADSM302 optical microscope and a Nikon microscope Eclipse using the 5x lenses, keeping the same focus and brightness during the whole study. The line width was calculated using ImageJ software, calibrating the scale using a SEM image of a TEM grid.

The SEM analysis was performed by an XHRSEM Magellan 400L Thermo Fisher Scientific microscope. The images were collected operating in a high vacuum with an electron beam energy of 2 kV and secondary electrons in-lens detector. The EDX mapping was performed right after taking the pictures increasing the energy to 6 kV and looking for gold, carbon, oxygen, nitrogen, and sodium elements.

Transmission electron microscopy (TEM) images and energy dispersive X-ray (EDX) spectra were acquired on an FEI Tecnai G2 F20 HRTEM coupled to an EDAX super ultra-thin window (SUTW) X-ray detector.

The XPS analysis was performed at room temperature by a SPECS PHOIBOS 150 hemispherical analyzer (SPECS GmbH, Berlin, Germany) with a base pressure of 5×10^{-10} mbar using monochromatic A1 K alpha radiation (1486.74 eV) as excitation source, with a power of 300 W. The energy resolution was 0.62 eV, as measured by the full width at half maximum (FWHM) of the Ag $3d_{5/2}$ peak for sputtered silver foil. The spectra were calibrated using C 1s at 284.8 eV as reference. The data analysis and fitting were performed using CasaXPS software. The constructed peak model was defined by using a Voigt function, with a Shirley background for the Au 4f. The peak model for the carbon peak was defined using a Gaussian-Lorentzian function, with no constraints on the peak position and keeping constant the ratio between the peak areas of the components.

The SERS measurements were performed by using a Renishow inVia confocal micro-Raman system, coupled with an optical Leica DLML microscope equipped with a NPLAN objective 20x with a numerical aperture of 0.75. The laser source used was a He-Ne laser at 633 nm. The spectrometer consists of a single grating monochromator (1800 lines mm^{-1}), coupled with a CCD detector, a RenCam 578×400 pixels (22 µm x 22 µm) cooled by a Peltier element. Spectral resolution of the spectrometer was 2.0 cm^{-1}. On the electrode surface was drop casted a Rhodamine B (purchased by Sigma Aldrich/Merck) solution $1*10^{-6}$ M in MilliQ water.

Electrical Characterizations–2-Point Probe Setup: The electrical resistance of the AuNPs printed lines was measured by a Keithley DMM6500 multimeter with standard probes, simply touching the pads at the two extremes of each line.

4-Point Probe Setup: In this work, pogo pin-type equidistant probes were used with a pressure of 120 g and a separation between them of 2.54 mm. A requirement for this technique was that the thickness of the film was less than 0.4 times the separation of the probes, which corresponds in this case to less than 1.016 mm. The probes were centered in the area to be measured (Figure S4, Supporting Information). Since the ratio between the side of the square (W) and the separation between probes (S) was less than 40, W/S = 20/2.54 = 7.87, it was necessary to apply a geometric correction reported in the literature (Haldor Topsøe, in Geometric Factors in Four Point Resistivity Measurement 1966). In this work, the correction factor used (C) for a W/S = 7.5 was C = 0.8846. Under these conditions, the sheet resistivity R_{sq} was given by Equation 1:

$$R_{sq} = \frac{\pi}{\ln(2)} \cdot C \cdot \left(\frac{\Delta V}{I}\right) = 4\left(\frac{\Delta V}{I}\right) \tag{1}$$

where ($\Delta V/I$) is the value reported by the multimeter.

AFM of the Thickness: AFM images were acquired using a PicoSPM II atomic force microscope in tapping mode. Images were processed using Gwyddion software for obtaining the profiles, exported, plotted, and process on Origin. Values obtained for the thickness were obtained by subtracting the average of the base points from the average of the top points, for four total profiles.

Electrochemical Characterization: For all the electrochemical measurements, one connection pad of the described layout (see Device fabrication) had served as contact and the other as a working electrode. A reproducible working electrode area was obtained insulating the AuNPs connection line (between the two pads) with screen printing insulating paste. The three-electrode electrochemical cell was completed with an external standard reference (Ag/AgCl 3 M KCl) and counter (platinum wire) electrodes (CH Instruments). All the reagents for the redox probe solutions were purchased from Merck (Sigma–Aldrich) and prepared as following: equimolar quantities (5 mM) of potassium ferrocyanide ($K_4[Fe(CN)_6]\cdot 3H_2O$) and potassium ferricyanide ($K_3[Fe(CN)_6]$) were dissolved in an appropriate volume of PBS, pH 7.4. Methylene blue solution was prepared dissolving the MB into PBS, obtaining the mother solution with a formal concentration of 5 mM. The lower concentrations were obtained by serial dilution of the mother solution.

The electrochemical characterizations were performed using a PalmSens4 potentiostat and Ivium Octostat. CVs were performed in 5 mM ferro/ferricyanide in PBS, scanning the potential from −0.35 to 0.65 V with scan rates of 25, 49, 64, 81, 100, 144, 196, 289, 400, and 484 mV s^{-1}. The CVs in 0.1 M H_2SO_4 were performed using a scan rate of 100 mV s^{-1} using a scanning potential from 0 to 1.55 V.

Square wave voltammetry (SWV) was performed to obtain the methylene blue (MB) curve for the treated devices. SWV parameters used: equilibration time 10 s at 0.1 V, frequency 25 Hz, amplitude 25 mV, potential ranging from 0.1 to −0.5 V (vs Ag/AgCl), E step of 0.003 mV. The concentration of MB ranged from 100 nM to 1 mM.

Supporting Information

Supporting Information is available from the Wiley Online Library or from the author.

Conflict of Interest

The authors declare no conflict of interest.

Data Availaility Statement

The data that support the findings of this study are available from the corresponding author upon reasonable request.

Keywords

[1] M. Faraday, *Philos. Trans. R. Soc.* **1857**, *147*, 145.

[2] A. Corma, H. Garcia, *Chem. Soc. Rev.* **2008**, *37*, 2096.

[3] , *Chem. Rev.* **2012**, *112*, 2739.

[4] E. C. Dreaden, A. M. Alkilany, X. Huang, C. J. Murphy, M. A. El-Sayed, *Chem. Soc. Rev.* **2012**, *41*, 2740.

[5] H. Chen, L. Shao, Q. Li, J. Wang, *Chem. Soc. Rev.* **2013**, *42*, 2679.

[6] Y.-C. Yeh, B. Creran, V. M. Rotello, *Nanoscale* **2012**, *4*, 1871.

[7] C. Parolo, A. Sena-Torralba, J. F. Bergua, E. Calucho, C. Fuentes-Chust, L. Hu, R. Álvarez-Diduk, E. P. Nguyen, S. Cinti, D. Quesada-González, A. Merkoçi, *Nat. Protoc.* **2020**, *15*, 3788.

[8] C. Fuentes-Chust, C. Parolo, G. Rosati, L. Rivas, K. Perez-Toralla, S. Simon, I. de Lecuona, C. Junot, J. Trebicka, A. Merkoçi, *Adv. Mater.* **2021**, *33*, 2006104.

[9] G. Rosati, A. Idili, C. Parolo, C. Fuentes-Chust, E. Calucho, L. Hu, C. D. C. Castro E Silva, L. Rivas, E. P. Nguyen, J. F. Bergua, R. Álvarez-Diduk, J. Muñoz, C. Junot, O. Penon, D. Monferrer, E. Delamarche, A. Merkoçi, *ACS Nano* **2021**, *15*, 17137.

[10] J. B. Chen, H. Yousefi, C. R. Nemr, S. Gomis, R. Atwal, M. Labib, E. Sargent, S. O. Kelley, *Adv. Funct. Mater.* **2020**, *30*, 1907701.

[11] A. N. Koya, X. Zhu, N. Ohannesian, A. A. Yanik, A. Alabastri, R. Proietti Zaccaria, R. Krahne, W.-C. Shih, D. Garoli, *ACS Nano* **2021**, *15*, 6038.

[12] X. Lang, A. Hirata, T. Fujita, M. Chen, *Nat. Nanotechnol.* **2011**, *6*, 232.

[13] J. Wang, *Microchim. Acta* **2012**, *177*, 245.

[14] C. Hu, X. Bai, Y. Wang, W. Jin, X. Zhang, S. Hu, *Anal. Chem.* **2012**, *84*, 3745.

[15] A. Määttänen, P. Ihalainen, P. Pulkkinen, S. Wang, H. Tenhu, J. Peltonen, *ACS Appl. Mater. Interfaces* **2012**, *4*, 955.

[16] F. Jia, C. Yu, Z. Ai, L. Zhang, *Chem. Mater.* **2007**, *19*, 3648.

[17] Y. Deng, W. Huang, X. Chen, Z. Li, *Electrochem. Commun.* **2008**, *10*, 810.

[18] K. Murata, K. Kajiya, M. Nukaga, Y. Suga, T. Watanabe, N. Nakamura, H. Ohno, *Electroanalysis* **2010**, *22*, 185.

[19] M. Saito, A. Kitamura, M. Murahashi, K. Yamanaka, L. Q. Hoa, Y. Yamaguchi, E. Tamiya, *Anal. Chem.* **2012**, *84*, 5494.

[20] D.-P. Song, A. Naik, S. Li, A. Ribbe, J. J. Watkins, *J. Am. Chem. Soc.* **2016**, *138*, 13473.

[21] L. P. Hernández-Saravia, A. Sukeri, M. Bertotti, *Int. J. Hydrogen Energy* **2019**, *44*, 15001.

[22] N. Xing, L. Lian, Y. Liu, Y. Shi, *Mater. Lett.* **2019**, *254*, 125.

[23] P. Varasteanu, C. Romanitan, A. Bujor, O. Tutunaru, G. Craciun, I. Mihalache, A. Radoi, M. Kusko, *Nanomaterials* **2020**, *10*, 2321.

[24] S. Nasrollahi, S. M. Ghoreishi, A. Khoobi, *J. Electroanal. Chem.* **2020**, *864*, 114097.

[25] J. A. Hondred, Z. T. Johnson, J. C. Claussen, *J. Mater. Chem. C* **2020**, *8*, 11376.

[26] Y. Xu, X. Wang, H. Chen, L. Chen, W. Chen, X. Yin, A. Liu, X. Lin, S. Weng, Y. Zheng, *J. Electroanal. Chem.* **2021**, *886*, 115109.

[27] P. Sondhi, D. Neupane, J. K. Bhattarai, A. V. Demchenko, K. J. Stine, *J. Electroanal. Chem.* **2022**, *924*, 116865.

[28] Q. Wan, J. Li, Z. Liu, L. Han, S. Huang, Z. Wang, *Metals* **2023**, *13*, 1255.

[29] D. Mcmanus, S. Vranic, F. Withers, V. Sanchez-Romaguera, M. Macucci, H. Yang, R. Sorrentino, K. Parvez, S.-K. Son, G. Iannaccone, K. Kostarelos, G. Fiori, C. Casiraghi, *Nat. Nanotechnol.* **2017**, *12*, 343.

[30] G. Hu, T. Albrow-Owen, X. Jin, A. Ali, Y. Hu, R. C. T. Howe, K. Shehzad, Z. Yang, X. Zhu, R. I. Woodward, T.-C. Wu, H. Jussila, J.-B. Wu, P. Peng, P.-H. Tan, Z. Sun, E. J. R. Kelleher, M. Zhang, Y. Xu, T. Hasan, *Nat. Commun.* **2017**, *8*, 278.

[31] C. J. Zhang, L. McKeon, M. P. Kremer, S. H. Park, O. Ronan, A. Seral-Ascaso, S. Barwich, C. Coileáin, N. McEvoy, H. C. Nerl, B. Anasori, J. N. Coleman, Y. Gogotsi, V. Nicolosi, *Nat. Commun.* **2019**, *10*, 1795.

[32] G. Rosati, M. Ravarotto, M. Scaramuzza, A. De Toni, A. Paccagnella, *Sensors Actuators, B Chem.* **2019**, *280*, 280.

[33] J. Frenkel, *J. Phys.* **1945**, *9*, 385.

[34] Y. Ge, X. Duan, M. Zhang, L. Mei, J. Hu, W. Hu, X. Duan, *J. Am. Chem. Soc.* **2018**, *140*, 193.

[35] J. Liu, Y. Ge, D. Zhang, M. Han, M. Li, M. Zhang, X. Duan, Z. Yang, J. Hu, *Nano Mater* **2021**, *4*, 1664.

[36] G. Maroli, S. Boyeras, H. Giannetta, S. Pazos, J. Gak, A. R. Oliva, M. A. Volpe, P. M. Julian, F. Palumbo, *Front. Electron.* **2023**, *3*, 1060197.

[37] J. R. Greer, R. A. Street, *Acta Mater.* **2007**, *55*, 6345.

[38] S. Wünscher, R. Abbel, J. Perelaer, U. S. Schubert, *J. Mater. Chem. C* **2014**, *2*, 10232.

[39] H. W. Tan, J. An, C. K. Chua, T. Tran, *Adv. Electron. Mater.* **2019**, *5*, 1800831.

[40] S.-H. Park, H.-S. Kim, *Thin Solid Films* **2014**, *550*, 575.

[41] J. Perelaer, R. Abbel, S. Wünscher, R. Jani, T. Van Lammeren, U. S. Schubert, *Adv. Mater.* **2012**, *24*, 2620.

[42] W. Gu, W. Yuan, T. Zhong, X. Wu, C. Zhou, J. Lin, Z. Cui, *RSC Adv.* **2018**, *8*, 30215.

[43] Y. Sui, Y. Dai, C. C. Liu, R. M. Sankaran, C. A. Zorman, *Adv. Mater. Technol.* **2019**, *4*, 1900119.

[44] S. Jang, H. Cho, S. Kang, S. Oh, D. Kim, *Appl. Phys. A Mater. Sci. Process.* **2011**, *105*, 685.

[45] D. D. Liana, B. Raguse, L. Wieczorek, G. R. Baxter, K. Chuah, J. J. Gooding, E. Chow, *RSC Adv.* **2013**, *3*, 8683.

[46] T. S.-W. Leung, E. Ramon, C. Martínez-Domingo, *Adv. Eng. Mater.* **2023**, *25*, 2200834.

[47] B. T. Anto, S. Sivaramakrishnan, L.-L. Chua, P. K. H. Ho, *Adv. Funct. Mater.* **2010**, *20*, 296.

[48] A. Gupta, S. Mandal, M. Katiyar, Y. N. Mohapatra, *Thin Solid Films* **2012**, *520*, 5664.

[49] L.-K. Lin, J.-T. Tsai, S. Díaz-Amaya, M. R. Oduncu, Y. Zhang, P.-Y. Huang, C. Ostos, J. P. Schmelzel, R. Mohammadrahimi, P. Xu, A. M. Ulloa Gomez, S. N. Shuvo, N. Raghunathan, X. Zhang, A. Wei, D. Bahr, D. Peroulis, L. A. Stanciu, *ACS Appl. Mater. Interfaces* **2021**, *13*, 11369.

[50] S. Magdassi, M. Grouchko, O. Berezin, A. Kamyshny, *ACS Nano* **2010**, *4*, 1943.

[51] Z. Li, K. S. Suslick, *Angew. Chemie. Int. Ed.* **2019**, *58*, 14193.

[52] M. J. Coutts, M. B. Cortie, M. J. Ford, A. M. Mcdonagh, *J. Phys. Chem. C* **2009**, *113*, 1325.

[53] D. Tobjörk, H. Aarnio, P. Pulkkinen, R. Bollström, A. Määttänen, P. Ihalainen, T. Mäkelä, J. Peltonen, M. Toivakka, H. Tenhu, R. Österbacka, *Thin Solid Films* **2012**, *520*, 2949.

[54] S. H. Ko, H. Pan, C. P. Grigoropoulos, C. K. Luscombe, J. M. J. Fréchet, D. Poulikakos, *Appl. Phys. Lett.* **2007**, *90*, 141103.

[55] H. Yamauchi, T. Dobashi, S. Sato, *Chem. Lett.* **2012**, *41*, 1154.

[56] A. M. Downs, J. Gerson, M. N. Hossain, K. Ploense, M. Pham, H.-B. Kraatz, T. Kippin, K. W. Plaxco, *ACS Sens.* **2021**, *6*, 2299.

[57] S. M. Ansar, F. S. Ameer, W. Hu, S. Zou, C. U. Pittman, D. Zhang, *Nano Lett.* **2013**, *13*, 1226.

[58] G. S. Perera, S. M. Ansar, S. Hu, M. Chen, S. Zou, C. U. Pittman, D. Zhang, *J. Phys. Chem. C* **2014**, *118*, 10509.

[59] H. I. Schlesinger, H. C. Brown, A. E. Finholt, J. R. Gilbreath, H. R. Hoekstra, E. K. Hyde, *J. Am. Chem. Soc.* **1953**, *75*, 215.

[60] R. Peña-Alonso, A. Sicurelli, E. Callone, G. Carturan, R. Raj, *J. Power Sources* **2007**, *165*, 315.

ADVANCED
SCIENCE NEWS

www.advancedsciencenews.com

NANO · MICRO
small
www.small-journal.com

[61] H. N. Abdelhamid, *Int. J. Hydrogen Energy* **2021**, *46*, 726.

[62] Y. Shang, R. Chen, *Energy Fuels* **2006**, *20*, 2142.

[63] V. G. Minkina, S. I. Shabunya, V. I. Kalinin, V. V. Martynenko, A. L. Smirnova, *Int. J. Hydrogen Energy* **2012**, *37*, 3313.

[64] D. Bhattacharjee, S. Dasgupta, *J. Mater. Chem. A* **2015**, *3*, 24371.

[65] S. Kumar, A. Jain, H. Miyaoka, T. Ichikawa, Y. Kojima, *Int. J. Hydrogen Energy* **2017**, *42*, 22432.

[66] X. Zhou, W. Xu, G. Liu, D. Panda, P. Chen, *J. Am. Chem. Soc.* **2010**, *132*, 138.

[67] J. C. Hoogvliet, M. Dijksma, B. Kamp, W. P. Van Bennekom, *Anal. Chem.* **2000**, *72*, 2016.

[68] S. P. Chenakin, N. Kruse, *Phys. Chem. Chem. Phys.* **2016**, *18*, 22778.

[69] Y. Borodko, S. E. Habas, M. Koebel, P. Yang, H. Frei, G. A. Somorjai, *J. Phys. Chem. B* **2006**, *110*, 23052.

[70] Y. Borodko, S. M. Humphrey, T. D. Tilley, H. Frei, G. A. Somorjai, *J. Phys. Chem. C* **2007**, *111*, 6288.

[71] I. Miguel-García, Á. Berenguer-Murcia, T. García, D. Cazorla-Amorós, *Catal. Today* **2012**, *187*, 2.

[72] J.-Y. Ye, G. A. Attard, A. Brew, Z.-Y. Zhou, S.-G. Sun, D. J. Morgan, D. J. Willock, *J. Phys. Chem. C* **2016**, *120*, 7532.

[73] J. García-Aguilar, M. Navlani-García, Á. Berenguer-Murcia, K. Mori, Y. Kuwahara, H. Yamashita, D. Cazorla-Amorós, *Langmuir* **2016**, *32*, 12110.

[74] J. Xian, Q. Hua, Z. Jiang, Y. Ma, W. Huang, *Langmuir* **2012**, *28*, 6736.

[75] G. Ruffato, F. Romanato, D. Garoli, S. Cattarin, *Opt. Express* **2011**, *19*, 13164.

[76] D. M. O. of N.-B. S. S. through L.-S. R. S. Solís, J. M. Taboada, F. Obelleiro, L. M. Liz-Marzán, F. J. García De Abajo, *ACS Photonics* **2017**, *4*, 329.

[77] J. Langer, D. Jimenez De Aberasturi, J. Aizpurua, R. A. Alvarez-Puebla, B. Auguié, J. J. Baumberg, G. C. Bazan, S. E. J. Bell, A. Boisen, A. G. Brolo, J. Choo, D. Cialla-May, V. Deckert, L. Fabris, K. Faulds, F. J. García De Abajo, R. Goodacre, D. Graham, A. J. Haes, C. L. Haynes, C. Huck, T. Itoh, M. Käll, J. Kneipp, N. A. Kotov, H. Kuang, E. C. Le Ru, H. K. Lee, J.-F. Li, X. Y. Ling, et al., *ACS Nano* **2020**, *14*, 28.

[78] P. Hildebrandt, M. Stockburger, *J. Phys. Chem.* **1984**, *88*, 5935.

[79] F. Tian, F. Bonnier, A. Casey, A. E. Shanahan, H. J. Byrne, *Anal. Methods* **2014**, *6*, 9116.

[80] M. Suzuki, Y. Niidome, Y. Kuwahara, N. Terasaki, K. Inoue, S. Yamada, *J. Phys. Chem. B* **2004**, *108*, 11660.

[81] S.-Y. Ding, J. Yi, J.-F. Li, B. Ren, D.-Y. Wu, R. Panneerselvam, Z.-Q. Tian, *Nat. Rev. Mater.* **2016**, *1*, 16021.

[82] R. L. Bard, L. R. Faulkner, H. S. White, *Electrochemical Methods: Fundamental and Applications*, John Wiley & Sons, Hoboken, New Jersey **2001**.

[83] M. M. Collinson, *Hindawi* **2013**, https://doi.org/10.1155/2013/692484.

[84] J. Liu, S. Wagan, M. Dávila Morris, J. Taylor, R. J. White, *Anal. Chem.* **2014**, *86*, 11417.

[85] G. Rosati, M. Urban, L. Zhao, Q. Yang, C. De Carvalho Castro E Silva, S. Bonaldo, C. Parolo, E. P. Nguyen, G. Ortega, P. Fornasiero, A. Paccagnella, A. Merkoçi, *Biosens. Bioelectron.* **2022**, *196*, 113737.

[86] C. L. Sajti, R. Sattari, B. N. Chichkov, S. Barcikowski, *J. Phys. Chem. C* **2010**, *114*, 2421.

[87] C. L. Sajti, A. Barchanski, P. Wagener, S. Klein, S. Barcikowski, *J. Phys. Chem. C* **2011**, *115*, 5094.

[88] G. Rosati, M. Ravarotto, M. Sanavia, M. Scaramuzza, A. De Toni, A. Paccagnella, *Sens. Bio-Sensing Res.* **2019**, *26*, 100308.